

Liquid-solid transition in fully ionized hydrogen at ultra-high pressures

Elisa Liberatore,^{1,a)} Carlo Pierleoni,^{2,b)} and D. M. Ceperley^{3,c)}

¹Department of Physics, University of Rome "La Sapienza," P.le A. Moro 2, 00185, Rome Italy

²CNISM and Department of Physics, University of L'Aquila, Via Vetoio 10, I-67010 L'Aquila, Italy

³Department of Physics, National Center of Supercomputer Applications, University of Illinois at Urbana-Champaign, Illinois 61801, USA

(Received 21 December 2010; accepted 12 April 2011; published online 11 May 2011)

We study the phase diagram of an effective ion model of fully ionized hydrogen at ultra-high pressure. We assume that the protons interact with a screened Coulomb potential derived from a static linear response theory. This model accurately reproduces the physical properties of hydrogen for densities greater than $\rho_m = 10 \text{ g/cm}^3$ corresponding to the range of the coupling parameter $r_s \lesssim 0.6$. The pressure range, $P \gtrsim 20 \text{ TPa}$, is well beyond present experimental limitations. Assuming classical protons, we find that the zero temperature enthalpy of the perfect bcc crystal is slightly lower than for other structures at $\rho_m = 12.47 \text{ g/cm}^3$ while the fcc structure gains stability at higher density. Using Monte Carlo calculations, we compute the free energy of various phases and locate the melting transition versus density. We find that on melting, bcc is energetically favored with respect to fcc over the entire range investigated. In the solid phase the system undergoes a structural transition from bcc at higher temperature to fcc at lower temperature. The free energy difference between these two structures is very small so that obtaining a quantitative estimate of this second transition line requires accuracy beyond that provided by our method. We estimate the effect of proton zero point motion on the bcc melting line for hydrogen, deuterium, and tritium by a path integral Monte Carlo method. Although zero point effects on hydrogen are large, since the two competing phases (bcc and liquid) have locally similar environments, the effect on the melting line is small; the melting temperature for hydrogen is lowered by about 10% with respect to the classical value. © 2011 American Institute of Physics. [doi:10.1063/1.3586808]

I. INTRODUCTION

Because hydrogen is the simplest and most abundant element in the universe, its physical properties are of great interest both because of its place in the periodic table and for its relevance to planetary physics and inertial fusion applications.^{1–7} At low pressures and temperatures, hydrogen behaves as a halogen, forming an insulating phase of diatomic molecules. Upon increasing pressure, well beyond the metallization pressure of 0.25 GPa predicted in 1935,⁶ a rich phase diagram has been observed with three different insulating molecular phases^{2,10} and a metallic liquid phase at higher temperature.⁷ Our current knowledge of the hydrogen phase diagram, based on limited experimental data and on theoretical predictions, e.g., *ab initio* simulations, is that at low temperature, below 500–800 K, solid hydrogen remains insulating and in the molecular phase up to $\approx 400 \text{ GPa}$.⁸ This pressure is slightly above the present limitation of modern experimental high-pressure static compression techniques.⁹ Upon increasing temperature, the freely rotating molecular hcp crystal melts to an insulating molecular liquid. The melting temperature increases with pressure up to $P \simeq 100 \text{ GPa}$ to a value of $T \simeq 800 \text{ K}$ and then

apparently decreases. At temperatures above the melting line, a liquid-liquid phase transition is predicted to occur between an insulating, mostly, molecular liquid and a conducting, mostly, atomic liquid.^{11–20} There has been a long-standing debate whether this process occurs in a continuous or through a first order transition. Indeed, the first Car-Parrinello simulations^{11,12} as well as calculations based on semi-empirical models^{15–19} showed the evidence of a discontinuous liquid-liquid transition, at variance with early Born-Oppenheimer molecular dynamics (BOMD) simulations and quantum Monte Carlo (QMC) investigations²¹ that found this process continuous. There is recent experimental evidence of a sharp conductivity rise.²² Moreover, the most recent and accurate *ab initio* QMC (Ref. 20) and BOMD (Refs. 13 and 20) calculations agree with the presence of a first order liquid-liquid transition. The QMC investigation by Morales *et al.*²⁰ predicts that the liquid-liquid transition terminates in a critical point at $T \simeq 2000 \text{ K}$, above which the metallization and the molecular dissociation with pressure occur in a continuous fashion. In the (P,T) plane, both the melting line and the metallization line have negative slopes and are predicted to meet at $T \simeq 550 \text{ K}$ and $P \simeq 290 \text{ GPa}$.²⁰ Qualitatively similar results are obtained by *ab initio* molecular dynamics simulations²⁰ which locate the intersection of the melting line with the metallization line at lower $T \simeq 700 \text{ K}$ and $P \simeq 220 \text{ GPa}$. A previous estimate of such intersection point by Car-Parrinello molecular dynamics was reported to be $T \simeq 400 \text{ K}$ and $P \simeq 300 \text{ GPa}$.¹²

a) Electronic mail: Elisa.Liberatore@roma1.infn.it.

b) Electronic mail: carlo.pierleoni@quila.infn.it.

c) Electronic mail: ceperley@illinois.edu.

At higher pressure, well beyond metallization and dissociation, hydrogen will be a metal of protons and delocalized electrons. Knowledge of the melting temperature of the atomic crystal is needed to understand the high pressure phase diagram. However, the stable crystal structures as a function of pressure and temperature are not known. Ground state quantum Monte Carlo investigations^{23–25} have estimated the transition from molecular to atomic crystal at $r_s = 1.31$ ($P = 300$ GPa)²³ and predicted a diamond structure to be the most stable at this density. *Ab initio* molecular dynamics with classical protons²⁶ have found that at high density ($r_s \leq 0.6$) and low temperature close packed structures such as fcc and hcp are dynamically stable while bcc to be dynamically stable at lower density ($0.6 \leq r_s \leq 1.2$). Moreover, the bcc phase was found to be the most stable phase at higher temperature and hence the phase that melts into the liquid. The melting temperature, estimated by Lindemann ratio criterium, was found to be $T_m = 2200$ K at $r_s = 0.5$ and $T_m = 350$ K at $r_s = 1$. In addition, it was suggested that linear response theory should be quantitatively correct for $r_s \lesssim 0.5$, since it provides an accurate prediction for the electronic density around a proton.

A very recent calculation used²⁷ random structure searching to find the optimal zero temperature structure within the assumed DFT energy functional. Several novel structures were found at intermediate densities. For example, I4₁/amd was found to be stable for $r_s > 1.0$ and the R-3m structure at higher density. For $r_s < 0.92$ fcc was found to be the most stable structure. Estimates were made for the contribution of phonons and finite temperature, indicating that although zero point effects can shift the transition densities, these structures, or closely related ones, should remain stable. Since the densities considered in this work are even higher, we only consider simple structures in this work.

The intermediate pressure region between the low pressure molecular phase and the high pressure, fully ionized phase, should present very interesting physics: molecular dissociation and metallization in the crystal phase, competition between crystal and liquid phases, and possible exotic liquid phases.²⁸ This region is still largely unknown since it is particularly challenging for both *ab initio* simulation techniques and experiment.

In this paper we study the melting of hydrogen at ultra-high density, corresponding to $0.6 \geq r_s \geq 0.3$. In our model, the ion-ion interaction is given by a screened Coulomb repulsion. We determine the melting line by calculating the free energy, both for classical and quantum protons and for the other isotopes of hydrogen. As suggested in Ref. 26, we find a competition between fcc and bcc structures below the melting temperature.

The paper is organized as follows. In Sec. II, we describe the model adopted in our study. Section III is devoted to the details of our calculations, in particular to the free energy method. We find a very small volume jump across the melting transition requiring a novel thermodynamic integration procedure described in the last part of Sec. III. In Sec. IV we derive the quantum correction to the free energy of the classical system and present our results. Finally, in Sec. V, we draw our conclusions and give some perspectives.

II. THE SCREENED COULOMB PLASMA MODEL

The screened coulomb plasma model has been introduced²⁹ as a model for a fully ionized plasma at weak coupling (high density). Its full derivation can be found in Ref. 30. Here we summarize the main steps and limit ourselves to the case of hydrogen. Consider a system of non-relativistic N_p protons and $N_e = N_p$ electrons in a volume V. The ionic (electronic) density is $n_p = n_e = n = N/V$. Denoting the coordinates of protons by $\{\mathbf{R}_1, \dots, \mathbf{R}_N\}$ and the coordinates of electrons by $\{\mathbf{r}_1, \dots, \mathbf{r}_N\}$, the Hamiltonian of the system is

$$\mathcal{H} = \mathcal{H}_{OCP} + \mathcal{H}_{eg} + \mathcal{V}_{int}, \quad (1)$$

$$\mathcal{H}_{OCP} = \mathcal{K}_p + \frac{1}{2V} \sum_{\mathbf{k} \neq 0} \hat{v}(k) [\rho_{\mathbf{k}}^p \rho_{-\mathbf{k}}^p - N], \quad (2)$$

$$\mathcal{H}_{eg} = \mathcal{K}_e + \frac{1}{2V} \sum_{\mathbf{k} \neq 0} \hat{v}(k) [\rho_{\mathbf{k}}^e \rho_{-\mathbf{k}}^e - N], \quad (3)$$

$$\mathcal{V}_{int} = -\frac{1}{2V} \sum_{\mathbf{k} \neq 0} \hat{v}(k) [\rho_{\mathbf{k}}^p \rho_{-\mathbf{k}}^e + c.c.], \quad (4)$$

where $k = |\mathbf{k}|$, $\hat{v}(k) = 4\pi/k^2$ is the Fourier transform of the Coulomb potential, $\rho_{\mathbf{k}}^p = e \sum_{i=1}^N \exp(i\mathbf{k} \cdot \mathbf{R}_i)$, $\rho_{\mathbf{k}}^e = -e \sum_{i=1}^N \exp(i\mathbf{k} \cdot \mathbf{r}_i)$ are the Fourier components of the charge density of protons and electrons, respectively, and \mathcal{K}_p and \mathcal{K}_e are the kinetic energy operators for protons and electrons, respectively. \mathcal{H}_{OCP} is the Hamiltonian of the one component plasma (OCP),³¹ a system of protons in a rigid background of negative neutralizing charge, \mathcal{H}_{eg} is the Hamiltonian of the electron gas (jellium),^{32,33} a system of electrons in a rigid background of positive neutralizing charge and \mathcal{V}_{int} is the interaction term between the two species (*c.c.* in Eq. (4) indicates complex conjugation). At high density \mathcal{V}_{int} becomes a weak coupling between the two systems.

We reduce the two component system to an effective one component system of pseudo-ions³⁰ by assuming the electronic degrees of freedom are in their instantaneous ground state for fixed ionic positions. If the coupling term is small, one can use linear response theory to express the electronic charge density in terms of the instantaneous ionic charge density; it is given by charge susceptibility of the homogeneous electron gas $\chi(k)$

$$\langle \rho_{\mathbf{k}}^e \rangle_e = -\hat{v}(k)\chi(k)\rho_{\mathbf{k}}^p = \left(\frac{1}{\varepsilon(k)} - 1 \right) \rho_{\mathbf{k}}^p, \quad (5)$$

where $\langle \dots \rangle_e$ is the average over the electronic ground state and $\varepsilon(k)$ is the dielectric function of the homogeneous electron gas. Using Eq. (5) in Eq. (1) gives the effective Hamiltonian for the ions

$$\begin{aligned} \mathcal{H}^{\text{eff}} &= \mathcal{H}_{OCP} + \frac{1}{2V} \sum_{\mathbf{k} \neq 0} \hat{v}(k) \left(\frac{1}{\varepsilon(k)} - 1 \right) [\rho_{\mathbf{k}}^p \rho_{-\mathbf{k}}^p - N] + E_{eg}(n) \\ &= \mathcal{K}_p + \frac{1}{2V} \sum_{\mathbf{k} \neq 0} \frac{\hat{v}(k)}{\varepsilon(k)} [\rho_{\mathbf{k}}^p \rho_{-\mathbf{k}}^p - N] + E_{eg}(n) \\ &= \mathcal{K}_p + \frac{1}{2} \sum_{i,j \neq i} v^{\text{eff}}(|\mathbf{R}_{ij}|; n) + E_{eg}(n), \end{aligned} \quad (6)$$

where $E_{eg}(n)$ is the ground state energy of the homogeneous electron gas with electronic density n , and $v^{\text{eff}}(R; n)$ is the Fourier transform of $[\hat{v}(k)/\epsilon(k)]$. Note that \mathcal{H}^{eff} depends on the density through both the volume term $E_{eg}(n)$ and the effective pair potential, $v^{\text{eff}}(R; n)$.

The energy and dielectric function of the homogeneous electron gas are well characterized.³³ Its ground state energy has been computed by quantum Monte Carlo methods³² and parameterized by several authors. We adopt the form of Perdew and Zunger,^{33,34} which at high density can be written as

$$\frac{E_{eg}(r_s)}{N} \simeq \frac{1.105}{r_s^2} - \frac{0.468}{r_s} + A \ln(r_s) + B + C r_s \ln(r_s) + D r_s, \quad (7)$$

where energy is in atomic units (1 a.u. = 27.2 ev = 315.79×10^3 K) and r_s is the electron sphere radius (the radius of the sphere containing one electron, in units of the Bohr radius a_0) defined as $r_s = (3/4\pi n)^{(1/3)}$. In Eq. (7) the first two terms are the Hartree-Fock contributions to the energy while the remaining terms represent the correlation energy $\epsilon_c(r_s)$. The values of the parameters are^{33,34} $A = 0.031$, $B = -0.048$, $C = 0.002$, $D = -0.0116$. The dielectric function is given by³³

$$\epsilon^{-1}(k) = 1 + \frac{\hat{v}(k)\mathcal{L}(k)}{1 - \hat{v}(k)\mathcal{L}(k)(1 - G(k))}, \quad (8)$$

where $\mathcal{L}(k)$ is the static Lindhard function, i.e., the susceptibility of the ideal Fermi gas. The local field factor $G(k)$ is proportional, through the interaction potential $\hat{v}(k)$, to the Fourier transform of the second functional derivative of the correlation energy functional with respect to the density.³⁵ Using quantum Monte Carlo methods, $G(k)$ has been computed in a range of density corresponding to $2 \leq r_s \leq 10$ and parameterized.^{33,35,36} Since our system is at higher density, i.e., at lower correlation, we expect that the local density approximation (LDA) form of $G(k)$ be accurate enough for our purpose³⁷

$$G(q) = q^2 \left[1 - \frac{\pi}{3} \left(\frac{4}{9\pi} \right)^{1/3} \left(r_s^3 \frac{d^2 \epsilon_c}{dr_s^2} - 2r_s^2 \frac{d\epsilon_c}{dr_s} \right) \right], \quad (9)$$

where ϵ_c is the correlation energy (i.e., the last 4 terms in Eq. (7)), $q = k/(2k_F)$ and k_F is the Fermi wave vector.

In Fig. 1 we show the effective potential for densities from $r_s = 0.435$ to $r_s = 0.6$. Note that Friedel oscillations are evident even at these high densities.

From the density dependence of the effective Hamiltonian, there are additional terms in the expression for the pressure.^{30,38} If \mathcal{F} is the Helmholtz free energy of the pseudions system, we have

$$\begin{aligned} p &= - \left(\frac{\partial \mathcal{F}}{\partial V} \right)_T = k_B T \frac{\partial}{\partial V} \log [Tr(e^{-\beta \mathcal{H}^{\text{eff}}})] \\ &= \frac{2\langle \mathcal{K}_p \rangle}{3V} - \frac{1}{6V} \left\langle \sum_{i,j \neq i} \left[|\mathbf{R}_{ij}| \frac{\partial v^{\text{eff}}(|\mathbf{R}_{ij}|; r_s)}{\partial |\mathbf{R}_{ij}|} \right. \right. \\ &\quad \left. \left. - r_s g^{\text{eff}}(|\mathbf{R}_{ij}|; r_s) \right] \right\rangle + p_{eg}(r_s), \end{aligned} \quad (10)$$

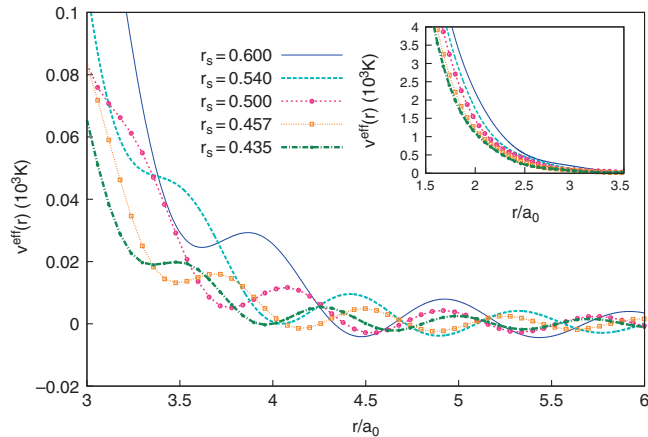


FIG. 1. The effective pair potentials $v^{\text{eff}}(r)$, for densities in the range $r_s \in [0.4, 0.6]$. The inset shows the short-range repulsive part of the linear response potential.

where $\langle \dots \rangle = Tr[e^{-\beta \mathcal{H}^{\text{eff}}} \dots]$, $g^{\text{eff}} = \partial v^{\text{eff}} / \partial r_s$ is the density derivative of the potential and the last term is the electron gas contribution

$$\begin{aligned} p_{eg}(r_s) &= -\frac{r_s}{3V} \frac{\partial E_{eg}(r_s)}{\partial r_s} = -\frac{1}{4\pi r_s^2} \left[-\frac{2.210}{r_s^3} + \frac{0.468}{r_s^2} \right. \\ &\quad \left. + \frac{A}{r_s} + C \ln(r_s) + D \right], \end{aligned} \quad (11)$$

$\langle \mathcal{K}_p \rangle = 3Nk_B T/2$ is the free particle contribution to the pressure.

To assess the validity of the linear response model we compare the electron-proton correlation function $h_{ep}(r) = g_{ep}(r) - 1 = \langle \sum_{i,J} \delta(\mathbf{r} - \mathbf{r}_i + \mathbf{R}_J) \rangle / (2N\rho) - 1$ for our pseudo-ion model against the one for the two component system of protons and electrons obtained by quantum Monte Carlo simulations in Fig. 2. In both cases the protons are kept fixed on the lattice sites of an fcc crystal. The correlation function $h_{ep}(r)$ is computed from the proton-proton static structure factor $S_{pp}(k) = \langle \rho_{\mathbf{k}}^p \rho_{-\mathbf{k}}^p \rangle / N$ by

$$h_{ep}(r) = \frac{1}{\rho} \int \frac{d\mathbf{k}}{(2\pi)^3} S_{pp}(\mathbf{k}) \left(\frac{1}{\epsilon(k)} - 1 \right). \quad (12)$$

The QMC data are obtained using variational Monte Carlo with a Backflow-Slater-Jastrow trial function with DFT-LDA single electron orbitals and optimized two-body correlation factors as described in Ref. 40. The linear response model is found to reproduce accurately the electron-proton correlation except close to the origin where the electron-proton cusp is rounded. The model becomes more accurate for increasing density and, as shown in the figure, for $r_s \leq 0.6$ it provides a very good approximation to the two component system.

III. CLASSICAL SIMULATIONS AND FREE ENERGY CALCULATION

The main aim of our work is to trace the melting line of hydrogen under conditions where the pseudo-ion effective model is appropriate. At these extreme pressures, quantum effects on the protons are relevant; we will consider both

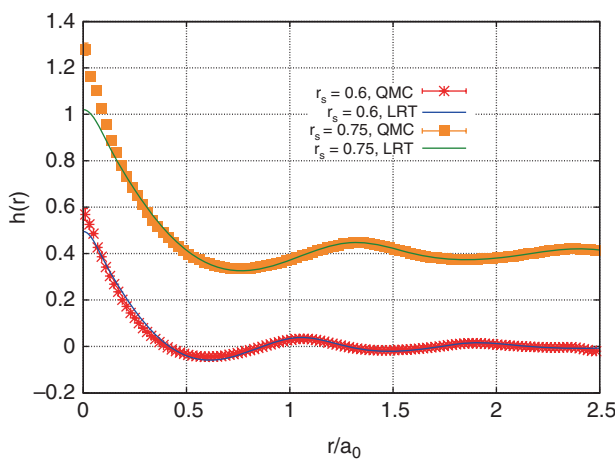


FIG. 2. Electron-proton correlation function $h_{ep}(r)$ at $r_s = 0.75$ and $r_s = 0.6$. Comparison between QMC data and the linear response prediction. Data at $r_s = 0.75$ has been shifted upward by 0.4 for the sake of clarity.

classical and quantum ions. In this section, we describe our strategy for the classical system and present results for the melting line. In Sec. IV, we incorporate quantum effects on the melting line. We have explored the interval of the coupling parameter $r_s \in [0.6, 0.435]$, corresponding to the density range $\rho_m [\text{g/cm}^3] \in [12.475, 32.736]$.⁵⁸

A. Ground state structure

To determine the ground state solid structure we computed the energy (enthalpy) as a function of density (pressure) for a number of different Bravais lattices, in particular, those found in previous works.^{23–25} We included cubic structures (face-centered, body-centered, simple cubic, the diamond, and A15 structures), hexagonal (simple and close packed) and orthorhombic (simple and body centered tetragonal, β -Sn structure). Simple and body centered tetragonal are simple and body centered cubic stretched along the z-direction, respectively. For those structures, the cell geometry depends on a single parameter $\gamma = c/a$: the ratio between the horizontal (a) and the vertical (c) cell sides. For those structures we computed the energy and the enthalpy for several values of γ and we found that the minimum energy and enthalpy is given by the cubic arrangement: $\gamma = 1$.

As shown in Fig. 1, the effective pair potential is repulsive at short distances with a small amplitude, slowly decaying, oscillating tail at larger distances: ($\sim \cos(k_f r + \phi)/r^3$). Because of the tail, the energy converges slowly as a function of the potential cut-off. The upper panel of Fig. 3 shows that the Madelung energy requires a very large cut-off, of the order of $80 - 90a_0$, to converge. However, we are interested in the energy, or enthalpy, difference between different structures, and this converges with a smaller cut-off of $20a_0$. (see the bottom panel of Fig. 3).

Figure 4 shows the energy and enthalpy per particle, relative to the fcc lattice, of the various structures considered, and in Table I we report the numerical values. The fcc lattice is the most stable structure in the range of density considered except at the lowest density point, followed by bcc, hcp, and A15

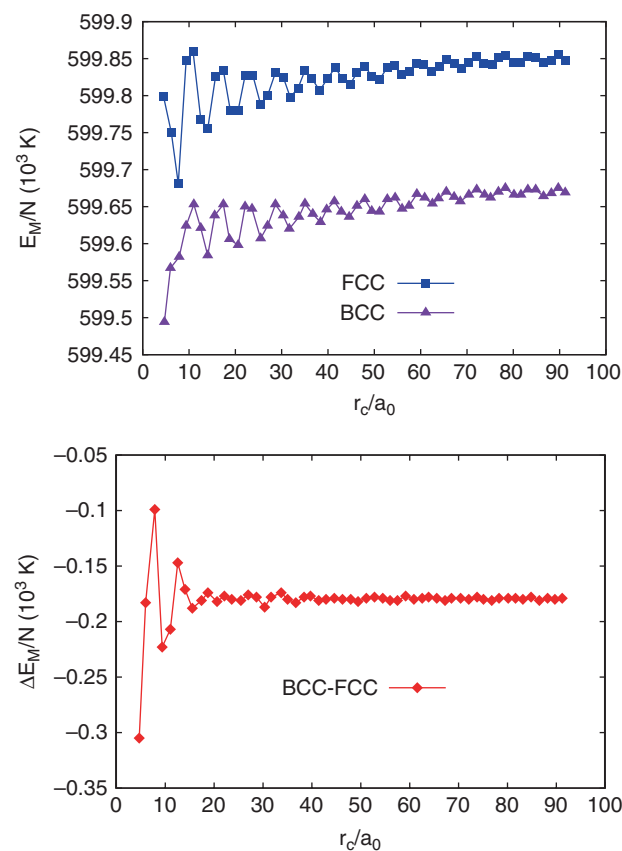


FIG. 3. Top panel: Convergence of the Madelung energy with respect to the potential cut-off r_c for the bcc and fcc structures at $r_s = 0.435$; bottom panel: convergence of the difference $E_{bcc} - E_{fcc}$ with respect to the potential cut-off.

structures. SH is considerably higher in energy and enthalpy while SC, diamond, and β -Sn structures are even higher and off-scale in Fig. 4.

B. Temperature behavior

Based on the ground state properties, we limit our investigation of the thermal behavior to the fcc and bcc structures only. To determine their relative stability with temperature and with respect to the liquid phase, we compute their free energies. To this aim we employed metropolis Monte Carlo in the NVT ensemble for temperatures $T \in [200, 5000]\text{K}$. Densities considered correspond to the Coulomb coupling parameter: $105 \leq \Gamma \leq 3630$, where $\Gamma = 1/(r_s T(\text{a.u.}))$. Previous investigations of the same model^{41–45} have been limited to values of $\Gamma \leq 150$, conditions relevant to high temperature plasmas in the interior of Jovian planets and in white and brown dwarfs.⁴¹ Properties were obtained by averaging over 40 000 MC passes (global moves), after a sufficiently long equilibration period.

Because of the oscillating tail of the potential, some care is needed in the energy calculation. For reasons of efficiency, we cut the pair potential at a distance $r_c = 6.2a_0$. The amplitude of the potential at the cut-off is only a few degrees Kelvin at all densities investigated, much less than the lowest temperature considered (200 K). To partially remove the

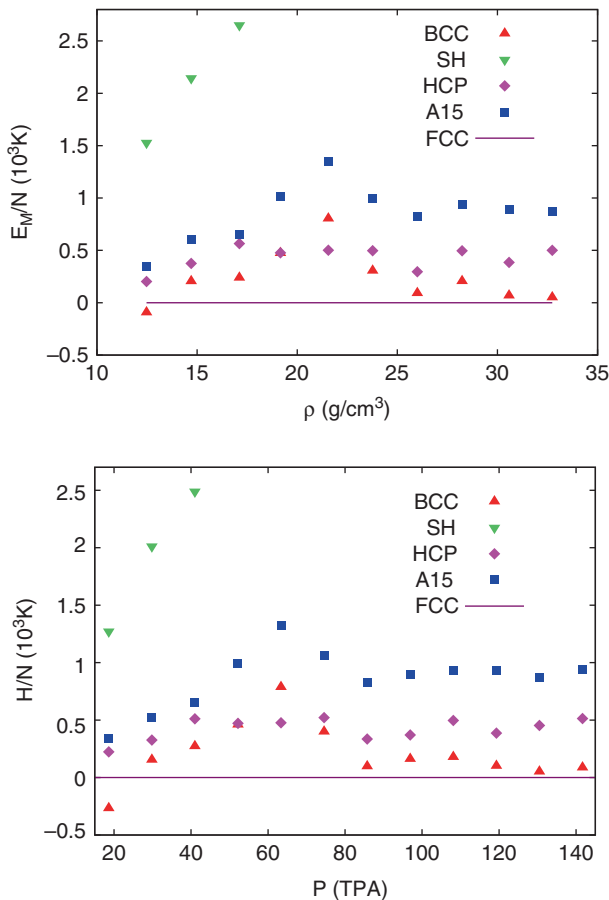


FIG. 4. Madelung energies (upper panel) and zero temperature enthalpies (lower panel) for different perfect lattices. Values are relative to the fcc phase. Data for less favorable structures (as β -Sn or diamond) are off the scale.

effect of the cutoff, we correct the energy by adding the difference between the converged value of the Madelung energy and that with the cut-off. In the liquid phase the standard tail correction,⁴⁷ obtained assuming $g(r) = 1$ for $r > r_c$ is used.

In order to use this cut-off radius and still work with a small number of ions in the simulation cell, we sum over interactions between particles in the primary simulation box as well as the 26 nearest images. With this strategy we are able to use $N \sim 250$ ions as compared with several thousands of ions if the box size were to be fixed at $L = 2r_c$. This procedure limits the maximum density that can be investigated

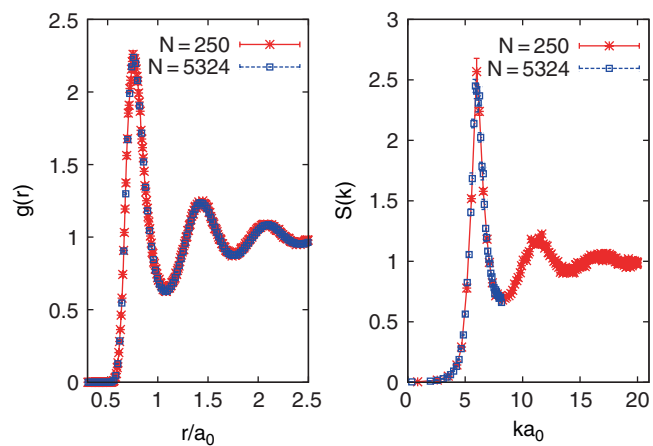


FIG. 5. Comparison between structural properties of small (256) and large (5324) systems: radial distribution function $g(r)$ (left) and structure factor $S(k)$ (right) at $T = 4000 \text{ K}$ and $r_s = 0.445$.

to $\rho \simeq 40 \text{ gr/cm}^3$ which corresponds to $r_s \simeq 0.41$. For higher densities (and lower r_s) we would need to use larger systems or sum over more neighboring boxes or to switch to the Ewald method. However, the use of the standard Ewald breakup for the linear response potential turns out not to be effective. We are presently investigating a different breakup, which will be employed in future studies. To check the effect of the artificial periodicity imposed by the nearest box images summation, we compare in Table II and Fig. 5, thermodynamic and structural properties computed with 256 particles in the liquid phase at $T = 4000 \text{ K}$ and different densities with those for a larger system ($N = 5324$) with box size $\gtrsim 2r_c$. We found a very good agreement for the radial distribution function, the structure factor, and the energies, but a small difference ($\approx 0.1\%$) in the pressure at higher densities. However, as explained in the following, the estimation of the transitions is based on the internal energy and not on the pressure.

C. Free energy calculations

A precise location of the melting line can be obtained from the Helmholtz free energy using the common-tangent construction.⁴⁶ it consists in plotting the isothermal free energy of the two competing phases as a function of the specific volume and finding pairs of points belonging to the

TABLE I. Converged Madelung energies for several crystalline structures as a function of density.

$\rho_m (\text{g/cm}^3)$	bcc	fcc	SC	A15	DIAM	hcp	SH
12.4753	258.813	258.961	263.856	259.707	276.966	259.143	260.770
14.7049	303.489	303.364	307.130	303.919	322.686	303.649	305.662
17.1130	343.393	343.274	349.423	344.064	364.410	343.995	345.915
19.1645	381.034	380.319	387.246	381.576	403.618	381.019	384.271
21.5574	423.440	422.495	427.607	423.421	447.825	423.623	426.830
23.7668	455.850	455.917	463.008	456.628	481.713	456.471	459.890
25.9999	496.124	495.991	503.589	496.813	522.661	496.378	500.259
28.2330	530.119	529.977	536.258	530.720	557.527	530.513	533.665
30.5792	566.214	566.138	573.469	567.185	594.810	566.590	570.061
32.7369	599.669	599.848	608.699	600.416	628.853	600.248	604.070

TABLE II. Comparison of energies per particle and pressures between a small system size ($N = 256$) summing over nearest box images, versus a large system size ($N = 5324$) with the minimum image convention. Calculations were for a liquid state at $T = 4000$ K and at various densities.

r_s	ρ_m (g/cm ³)	$E_{256}(10^3\text{K})$	$E_{5324}(10^3\text{K})$	$P_{256}V(10^3\text{K})$	$P_{5324}V(10^3\text{K})$
0.600	12.5	268.22(1)	268.237(2)	60.217(3)	60.210(1)
0.540	17.0	352.73(1)	352.730(2)	76.616(2)	76.614(1)
0.500	21.5	429.64(1)	429.647(2)	90.576(2)	90.6587(9)
0.484	23.7	466.40(1)	466.408(3)	98.969(2)	98.972(2)
0.468	26.3	503.42(1)	503.425(4)	107.225(2)	107.232(1)
0.457	28.2	539.02(2)	539.110(5)	112.818(1)	112.830(1)
0.445	30.5	575.84(2)	575.845(5)	118.392(3)	118.501(1)
0.435	32.7	609.09(1)	609.096(3)	126.032(2)	126.128(3)

different curves but lying on a common tangent. The abscissa of those points represents the specific volume of each phase at coexistence, while the slope of the tangent is the coexistence pressure. This procedure relies on hysteresis; in a simulation with a finite number of particles and a finite number of Monte Carlo steps, one can work in a metastable phase, since near a first order phase transition, there is a barrier for conversion of the MC random walk from a liquid configuration to a crystal configuration or vice versa.

Alternatively, the location of the transition can be obtained from the crossing point of the isothermal Gibbs free energy curves of the competing phases plotted against pressure. These curves can be obtained from the behavior of the Helmholtz free energy and the pressure as a function of volume. The dependence of the Gibbs free energy on pressure must be inferred by inverting the equation of state, a procedure which can introduce systematic errors, so that we preferred to use the Helmholtz free energy with the common tangent construction.

For each phase, the Helmholtz free energy can be obtained by thermodynamic integration⁴⁷ from a reference state, e.g., a coupling constant integration: one introduces a fictitious Hamiltonian dependent on a parameter $\lambda \in [0, 1]$ which couples the original system to a reference system of known (or easy-to-compute) free energy. If $\mathcal{H}_\lambda = \mathcal{H}_1\lambda + \mathcal{H}_0(1 - \lambda)$, where \mathcal{H}_1 is the Hamiltonian of the reference system and \mathcal{H}_0 the Hamiltonian of the original system, we have

$$\mathcal{F}(0) = \mathcal{F}(1) + \int_0^1 d\lambda \langle \mathcal{H}_0 - \mathcal{H}_1 \rangle_\lambda, \quad (13)$$

where $\langle \dots \rangle_\lambda$ indicates an average with respect to $e^{-\beta\mathcal{H}_\lambda}$. In the solid phase, a suitable reference system is an Einstein crystal of the same structure, in which each particle is attached to a lattice site with a spring (Frenkel-Ladd technique).^{47,48} For the liquid phase, we used the coupling parameter λ to switch off the interaction between the pseudo-ions $\mathcal{V}_\lambda = (1 - \lambda)\mathcal{V}^{\text{eff}}$. This is equivalent to increasing the temperature up to the ideal gas limit. The integrals over λ are estimated with a Gauss-Legendre quadrature scheme with 12 points for the solid phases and 20 points for the liquid phase. In the latter case, where the integrand has a cusp as λ approaches 1, a correction accounting for the inability of the Gauss-Legendre interpolants to follow the behavior of the integrand has been added to the estimate of the integral.⁴⁹

Thermodynamic integrations along isochores are carried out for each density and for the three phases by (1) computing the internal energies on a grid of temperatures, (2) fitting the energy data with a cubic polynomial in T , $U(T, \rho) = \sum_{n=0}^3 a_n(\rho)T^n$, and (3) performing the integration of the fitting function. We have integrated from 6000 K for the liquid phase and from 500 K for the solid phases. Numerical values for the fitting parameters a_n are reported in Table III. Along isotherms, the density dependence of the excess Helmholtz free energy can be fit with a second order polynomial in ρ_m . We obtain the pressure with small errors by differentiation.

Inset (a) of Fig. 6 shows an example of the excess Helmholtz free energies along the isotherm at $T = 2500$ K for the three phases: liquid, bcc, and fcc. The three curves are very close to each other and only slightly convex. In order to enhance their curvature, and to help in constructing a common tangent, we have subtracted from all curves the same linear behavior κv ; this does not affect the tangent construction. An example is given in the main panel of Fig. 6. A crossing point between the liquid and the bcc curves is now visible between $v = 0.45a_0^3$ and $v = 0.46a_0^3$. Even with this subtraction the common tangent construction is particularly hard to apply. Although our error bars on the free energy are very small ($\sim 0.003\%$), the free energy curves are so close to each other that an estimate of the volume change at coexistence is very difficult.

We interpreted this as an indication that the change of volume at coexistence is very small. A first order phase transition with no volume change does occur in the one component plasma because any volume discontinuity will cost an infinite energy due to the infinite range of the interaction potential and to the presence of a rigid neutralizing background. The linear response potential does have a finite range because of the polarizing background, so that a volume discontinuity is in principle possible, but probably very small. Assuming a negligible specific volume discontinuity at the coexistence between two phases α and β , the difference in Helmholtz free energy, $\Delta\mathcal{F}_{\alpha,\beta}$ and the difference in Gibbs free energy $\Delta\mathcal{G}_{\alpha,\beta}$ both vanish

$$\begin{aligned} \Delta\mathcal{G}_{\alpha\beta}(T, P) &= \mathcal{F}_\alpha(T, P(V_\alpha)) - \mathcal{F}_\beta(T, P(V_\beta)) + P(V_\alpha - V_\beta) \\ &= \Delta\mathcal{F}_{\alpha\beta}(T, P(V)) = 0. \end{aligned} \quad (14)$$

As a consequence, a transition is given by the intersection of the Helmholtz free energy curves, either along isotherms

TABLE III. Values of the parameters used to fit the internal energy of the bcc, the fcc, and the liquid phase, and the reference free energy.

$\rho(\text{g}/\text{cm}^3)$	12.5	17.0	21.5	23.7	26.3	28.2	30.5	32.7
$f_0^{\text{Liq}}(10^3 \text{ K})$	283.963	369.807	447.776	484.973	522.443	558.328	595.599	629.097
$a_0^{\text{Liq}}(10^3 \text{ K})$	261.106	344.778	421.768	458.798	494.198	536.023	567.483	599.164
$a_1^{\text{Liq}}(-)$	2.59492	3.02028	2.66867	2.36179	3.71206	-1.15905	2.79676	3.95242
$a_2^{\text{Liq}}(10^{-3} \text{ K}^{-1})$	-0.28690	-0.36262	-0.22277	-0.13043	-0.49238	0.74571	-0.05808	0.07058
$a_3^{\text{Liq}}(10^{-8} \text{ K}^{-2})$	2.02837	2.62222	1.1955	0.40000	3.5556	-6.66667	2.26667	3.54815
$f_0^{\text{fcc}}(10^3 \text{ K})$	265.192	349.350	425.924	462.543	499.655	535.112	571.897	604.990
$a_0^{\text{fcc}}(10^3 \text{ K})$	261.155	345.007	421.300	457.972	495.242	530.686	567.417	600.403
$a_1^{\text{fcc}}(-)$	1.35851	1.15098	2.11172	1.82019	1.45954	1.396	1.46372	1.44968
$a_2^{\text{fcc}}(10^{-3} \text{ K}^{-1})$	0.10355	0.32446	-0.40172	-0.18129	0.04134	0.08474	0.03438	0.14450
$a_3^{\text{fcc}}(10^{-8} \text{ K}^{-2})$	1.24273	-6.39716	10.4001	5.26667	0.58979	-0.39457	0.673656	-2.98644
$f_0^{\text{bcc}}(10^3 \text{ K})$	265.042	349.214	425.941	462.584	499.650	535.153	571.938	605.039
$a_0^{\text{bcc}}(10^3 \text{ K})$	261.032	345.108	421.513	457.977	495.277	530.863	567.907	600.478
$a_1^{\text{bcc}}(-)$	1.42007	1.10833	1.72589	2.02952	1.50003	1.16169	1.5467	1.51647
$a_2^{\text{bcc}}(10^{-3} \text{ K}^{-1})$	-0.02345	0.34584	-0.13167	-0.33069	-0.02288	0.23754	-0.29343	-0.51038
$a_3^{\text{bcc}}(10^{-8} \text{ K}^{-2})$	5.87915	-6.67735	4.16266	8.05108	2.18527	-3.81446	2.49272	-1.24264

or isochores, taking care to verify *a posteriori* that the pressure at coexistence is equal for the two phases. In panel (b) of Fig. 6 and in Fig. 7 we show an example of detecting a coexistence point along an isotherm and along an isochore, respectively.

In Fig. 8 we report our data for the melting line, together with the melting line of the one component plasma ($\Gamma = 178$).⁵⁰ As expected, we find that in the solid phase the bcc is more stable than the fcc at coexistence with the liquid and that the melting line is slightly concave with a melting temperature between 1500 and 3000 K in the explored density range. Numerical data for the melting line are summarized in Table IV together with the pressure for the solid and the liquid phases. On melting, the pressure for the two coexisting phases obtained from the density derivative of the free energy

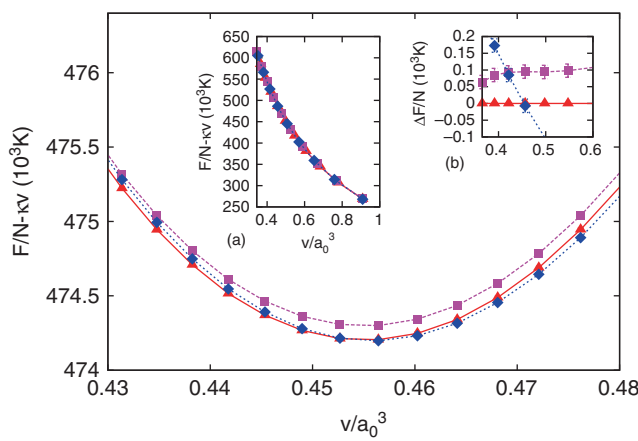


FIG. 6. Comparison of the Helmholtz free energy curves, as a function of the specific volume v , for bcc (red triangles), fcc (magenta squares) and liquid (blue diamonds) phases, along the isotherm $T = 2500 \text{ K}$. To enhance the curvature of the free energy lines, a linear term $l(v) = -\kappa v$, with $\kappa = 3.9 \times 10^6 \text{ K}/a_0^3$, has been added to each curve. A common tangent between the bcc and the liquid curves passes very near to their intersection, at $v \approx 0.453a_0^3$, but the construction is sensitive to errors. In inset (a) the behavior of the isothermal free energies is shown. In inset (b) fcc and liquid free energies relative to the bcc phase are plotted in order to highlight the differences.

at constant temperature are found to be in agreement within error bars, supporting the assumption that the transition occurs with a very small volume discontinuity.

Using the same procedure, we can make predictions for the bcc-fcc transition line. Indeed from the Madelung energies in Sec. III A, we expect that fcc becomes more favorable than bcc at low enough temperature. This is confirmed from the free energy curves along isochores which cross at low temperature. The resulting transition points are reported in Fig. 8. At variance with the bcc-liquid case, the free energy difference is now much smaller and statistical errors larger. Moreover, the transition points are more scattered with density than observed for the liquid-bcc transition, most probably because of the truncation of the potential adopted in our simulations which become more important at lower temperature. Nonetheless, our data indicate unambiguously the presence of a structural phase transition line with T between 250 and 1000 K in the density range $\rho_m(\text{g}/\text{cm}^3) \in [12.475, 32.736]$.

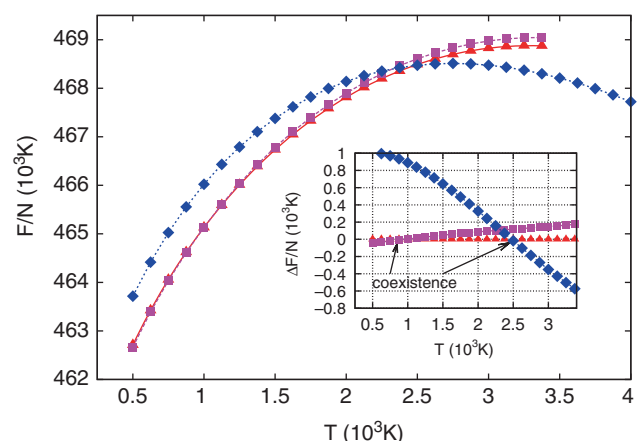


FIG. 7. Free energies per particle of the liquid (blue diamonds), fcc (magenta squares), and bcc (red triangles) phases, along the isochore at $\rho_m = 23.7 \text{ g}/\text{cm}^3$. Assuming a small volume discontinuity at transition, the coexistence points can be easily recognized as the intersection between the curves. Inset: free energies relative to the bcc phase. Errors are smaller than the size of the symbols.

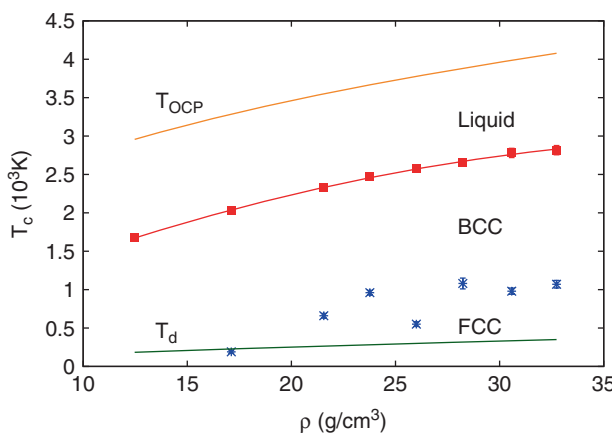


FIG. 8. Coexistence points for the liquid-bcc transition (red squares) and for the bcc-fcc transition (blue stars). Data points are obtained assuming no volume change between the two phases at the transition. The OCP melting line ($\Gamma = 178$) is represented by the orange line and the degeneracy temperature for protons (see Sec. IV) by the green line.

Finally we have investigated finite size effects on the transition, by computing internal energies versus N for the three phases considered. For both crystalline phases we have found that the specific free energy rises by roughly 30 K, while for the liquid phase size effects are negligible. As a consequence our estimate of the fcc-bcc transition is unaffected by size effects while the bcc-liquid temperature is lowered by an amount which is within the statistical uncertainties.

IV. NUCLEAR QUANTUM EFFECTS ON THE MELTING TRANSITION

So far we have considered the ions to be classical particles. However, at high density the quantum effects for protons might be relevant to the precise location of the transition lines. The relevance of quantum delocalization and statistics can be qualitatively understood by comparing to the degeneracy temperature $T_d = \frac{\hbar^2}{m_p k_B} n^{2/3}$, the temperature at which the thermal deBroglie wavelength equals the interparticle distance; m_p is the proton mass. As seen in Fig. 8, the degeneracy temperature is much lower than the melting temperature. In crystal phases, strong correlation between atomic motions typically reduces exchange effects by three or more orders of magnitude; effects of fermi or bose statistics should be negligible for the temperatures considered here. The quantum effects on the

TABLE IV. Estimates for the melting temperature T_m and pressure in the liquid (P_l) and bcc (P_{bcc}) phases.

ρ_m (g/cm ³)	T_m (10 ³ K)	P_l (TPa)	P_{bcc} (TPa)
12.5	1.68(4)	24.5(2)	24.7(2)
17.0	2.03(2)	42.1(2)	42.3(2)
21.5	2.33(3)	65.2(3)	65.5(3)
23.7	2.48(3)	81.0(4)	81.4(4)
26.3	2.57(3)	92.3(4)	92.8(4)
28.2	2.65(4)	103.3(4)	103.9(4)
30.5	2.78(6)	119.5(4)	120.1(4)
32.7	2.82(6)	136.3(4)	136.8(4)

phase transitions can only be due to zero point motion. Quantum effects on melting have been estimated for the quantum one component plasma and for a model of quantum protons interacting through a Thomas-Fermi potential.^{51,52} Since our present estimate of the fcc-bcc line is only qualitative, we will compute quantum correction to the melting line only.

A. Formalism

In order to determine the effect of zero point motion on the melting transition one can integrate the inverse mass $\lambda = \hbar^2/2m$ starting from the classical free energy, where $\lambda = 0$. The free energy derivative with respect to λ is given by³⁹

$$\frac{\partial \mathcal{F}_\lambda}{\partial \lambda} = \frac{1}{\lambda} \langle \hat{\mathcal{K}} \rangle_\lambda, \quad (15)$$

where $\langle \hat{\mathcal{K}} \rangle_\lambda = \langle -\lambda \nabla^2 \rangle_\lambda$ is the average kinetic energy of the quantum system of Hamiltonian $\hat{\mathcal{H}}_\lambda = -\lambda \nabla^2 + \hat{\mathcal{V}}$. The free energy of a system with given λ at a given thermodynamic condition (T, ρ), can then be obtained from the free energy of another system at the same thermodynamic point, with same potential energy but different mass, corresponding to λ_0 , by the integration formula

$$\mathcal{F}(\lambda_p) = \mathcal{F}(\lambda_0) + \int_{\lambda_0}^{\lambda_p} \frac{d\lambda}{\lambda} \langle \hat{\mathcal{K}} \rangle_\lambda. \quad (16)$$

When λ_0 becomes sufficiently small, the reference system can be approximated with its classical limit. By splitting the kinetic energy into a ideal and an excess part, we can rewrite the integration as

$$\begin{aligned} \mathcal{F}(\lambda_p) &= \mathcal{F}(\lambda_0) + \frac{3}{2} N K_B T \ln \left(\frac{\lambda_p}{\lambda_0} \right) \\ &\quad + \int_0^{\lambda_p} \frac{d\lambda}{\lambda} \left[\langle \hat{\mathcal{K}} \rangle_\lambda - \frac{3}{2} N K_B T \right] \\ &= \mathcal{F}_{cl}(\lambda_p) + \int_0^{\lambda_p} \frac{d\lambda}{\lambda} \left[\langle \hat{\mathcal{K}} \rangle_\lambda - \frac{3}{2} N K_B T \right], \end{aligned} \quad (17)$$

where $\mathcal{F}_{cl}(\lambda_p)$ is the free energy of the classical system with the actual value of $\lambda_p = \hbar^2/2m_p$. The lower bound of the integral has been extended to 0 since quantum deviation in the kinetic energy goes linearly with λ and cancels the divergence of the integrand at $\lambda = 0$. This procedure provides the quantum free energy for all isotopes at once.

In order to compute the quantum corrections [Eq. (17)] to the melting curve, we carried out path integral MC (PIMC) simulations in the NVT ensemble. The path integral formalism is based on the factorization $\exp(-\beta \hat{\mathcal{H}}) = [\exp(-\beta \hat{\mathcal{H}}/M)]^M$ of the density matrix $\hat{\rho}_\beta = \exp(-\beta \hat{\mathcal{H}})$ in the coordinate representation

$$\langle \mathbf{R} | \hat{\rho}_\beta | \mathbf{R}' \rangle = \rho(\mathbf{R}, \mathbf{R}' | \beta) = \int \prod_{i=1}^{M-1} d\mathbf{R}_i \prod_{i=1}^M \rho(\mathbf{R}_{i-1}, \mathbf{R}_i | \tau), \quad (18)$$

where $\mathbf{R}_0 = \mathbf{R}$ and $\mathbf{R}_M = \mathbf{R}'$. The integral is over all the possible paths of M intermediate steps and total length β ; $\tau = \beta/M$ is called the time slice. The advantage of this factorization is that for small enough τ it is possible to obtain accurate approximate expressions of the density matrices

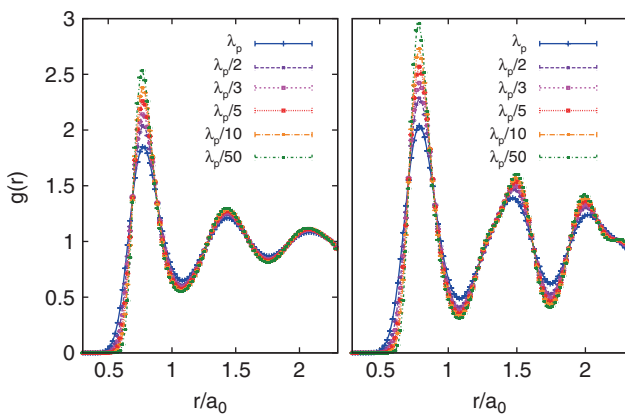


FIG. 9. Dependence of the radial distribution function on λ , for the liquid (left panel) and the bcc solid (right panel), near the classical melting temperature. $\rho_m = 30.5 \text{ g/cm}^3$ (corresponding to $r_s = 0.445$), $T = 2780 \text{ K}$. At the smaller value of λ , $\lambda = \lambda_p/50$, the $g(r)$ of the system is identical within errorbars to the $g(r)$ of the classical system. For quantum particles, the $g(r)$ becomes less structured and the height of the first peak is largely reduced with respect to the classical limit.

$\rho(\mathbf{R}_{i-1}, \mathbf{R}_i | \tau)$. For systems with a pair potential $v(r)$, an accurate form of $\rho(\mathbf{R}_{i-1}, \mathbf{R}_i | \tau)$, rapidly convergent with the time slice, is given by the pair density matrix.³⁹

We carried out a series of PIMC simulations at different densities in the range $\rho_m \in [12, 33] \text{ g/cm}^3$, corresponding to $r_s \in [0.435, 0.6]$. Since we expected the quantum effects on the melting temperature to be small, at each density ρ_m we only calculated the corrections to the free energies for three temperatures around the classical melting temperature $T_m^{cl}(\rho)$, for both the bcc and the liquid phases. We used systems of 250 protons with a potential cut-off radius of $r_c = 6.2a_0$. Both potential energy and pair actions have been obtained by considering each particle and its 26 nearest images. We used $M = 32$ time slices, which, according to tests, gives a satisfactory convergence ($\leq 3\%$) of the kinetic energy over the entire density range. Properties were averaged over 40 000 MC passes, after equilibration.

Figure 9 shows an example of the dependence of the radial distribution function $g(r)$ on λ , for both the bcc solid and the liquid phase. In both phases, the $g(r)$ peaks broaden as λ is increased and for $\lambda = \lambda_p$ the height of the first peak is 60% smaller than the classical one. In addition, the rise of the $g(r)$ is less steep and begins at shorter distances than does the classical system.

To estimate the integral over λ in Eq. (17), we use a grid of six values from λ_p down to $\lambda_p/20$ below which the kinetic energy follows the semiclassical linear behavior^{53,54}

$$\langle \hat{\mathcal{K}} \rangle_\lambda - \frac{3}{2} k_B T \approx \lambda \frac{\pi}{3} \frac{\rho}{K_B T} \int_0^\infty r^2 g_{cl}(r) \times \left[\frac{d^2 v^{\text{eff}}(r)}{dr^2} + \frac{2}{r} \frac{dv^{\text{eff}}(r)}{dr} \right] dr + O(\lambda^2), \quad (19)$$

where the $g_{cl}(r)$ is the radial distribution function of the classical system. The behavior of the integrand with λ , illustrated in Fig. 10, can be accurately fit with a cubic polynomial in λ : $\langle \hat{\mathcal{K}} \rangle_\lambda - \frac{3}{2} k_B T = \kappa_1 \lambda + \kappa_2 \lambda^2 + \kappa_3 \lambda^3$, which is then integrated to obtain the free energy of the quantum system. As we did

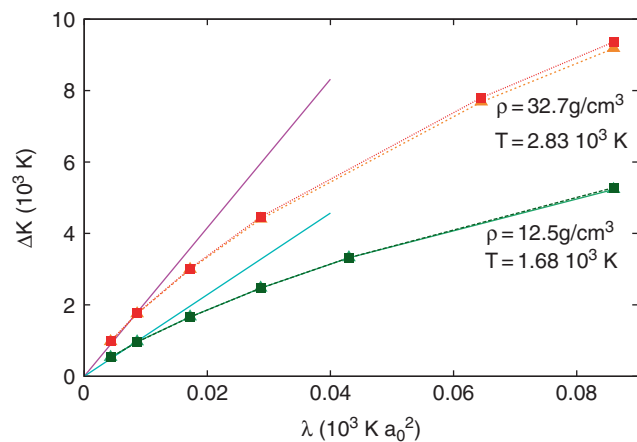


FIG. 10. Quantum contribution to the kinetic energies per particle of the liquid (triangles) and the bcc crystal (squares), as a function of λ , for the lowest density ($\rho_m = 12.5 \text{ g/cm}^3$, green lines) and the highest density ($\rho_m = 32.7 \text{ g/cm}^3$, red lines) considered, at the times classical melting temperature ($T_m = 1.68 \times 10^3 \text{ K}$ and $T_m = 2.82 \times 10^3 \text{ K}$, respectively). The straight lines show the semiclassical behavior valid at low λ from Eq. (19).

for classical melting, we assume that the volume discontinuities at coexistence can be neglected, so that the melting temperature at fixed density occurs when free energies of the two phases becomes equal. These values are summarized in Table V and illustrated in Fig. 11. Quantum effects on the melting are negligible ($\leq 2\%$) over the entire range of densities for tritium (T) and quite small ($\leq 4\%$) for deuterium (D), as shown in the inset of Fig. 11. For hydrogen, its melting temperature are lowered by as much as 10%; the melting curve is flattened at the highest densities considered.

We note that in the limit of high density, zero point effects will eventually cause the hydrogen lattice to melt, even at $T = 0$. At sufficiently high density the electron screening is ineffective so that $\epsilon(k) = 1$ in Eq. (6), and the protons interact with the bare coulomb interaction. Since the properties of any one-component system are only determined by the dimensionless coupling parameter, we can use the result of

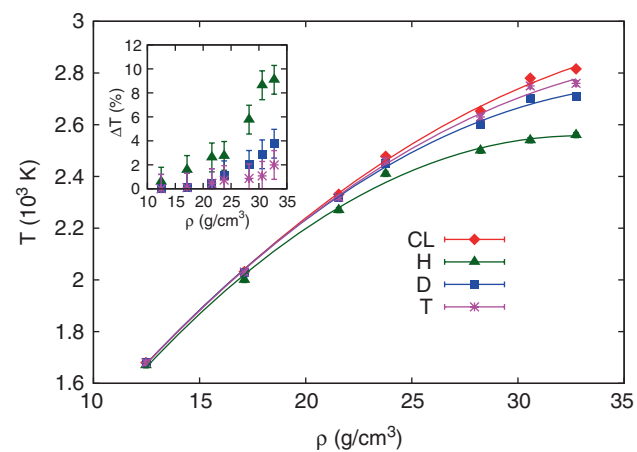


FIG. 11. Melting lines for hydrogen (H, green triangles), deuterium (D, blue squares) and tritium (T, magenta squares), and the classical melting curve (CL, red diamonds). Dashed lines show the polynomial fit of the data points. The inset shows differences in the melting temperatures between the classical and the quantum system.

TABLE V. The bcc-liquid transition temperature, as a function of the density, for classical protons ($T_m^{(cl)}$), tritium ($T_m^{(T)}$), deuterium ($T_m^{(D)}$), and hydrogen ($T_m^{(H)}$).

r_s	ρ_m (g/cm ³)	$T_m^{(cl)}$ (10 ³ K)	$T_m^{(T)}$ (10 ³ K)	$T_m^{(D)}$ (10 ³ K)	$T_m^{(H)}$ (10 ³ K)
0.600	12.5	1.68(4)	1.68(4)	1.68(4)	1.67(4)
0.540	17.0	2.03(2)	2.03(2)	2.03(2)	2.00(2)
0.500	21.5	2.33(3)	2.32(3)	2.32(3)	2.27(3)
0.484	23.7	2.48(3)	2.46(3)	2.45(3)	2.41(3)
0.457	28.2	2.65(4)	2.63(4)	2.60(4)	2.50(4)
0.445	30.5	2.78(6)	2.75(6)	2.70(6)	2.54(6)
0.435	32.7	2.82(6)	2.76(6)	2.71(6)	2.56(6)

QMC calculations of the 3D Wigner crystallization of electrons for spin 1/2 fermions. It has been found^{32,55} that the critical density is $r_s^*(e) = 106$. Scaling this value using the ratio of electron to proton mass we find $r_s^*(p) = (m_e/m_p)r_s^*(e) = 0.0578(6)$. A rough estimate of the effect of including some electronic screening suggests that the zero temperature high density melting transition could occur at a somewhat lower density: $r_s^* = 0.1$.⁵⁶ Further calculations are needed to firm up this estimate.

V. CONCLUSION

In this paper we have investigated fully ionized hydrogen in a range of densities between 12 g/cm³ and 32 g/cm³ corresponding to the range of electronic Coulomb coupling parameter $r_s \in [0.43, 0.6]$ and the range of pressure $24 T\text{Pa} \leq p \leq 140 T\text{Pa}$ where the electrons are weakly coupled to the proton charges and screen the bare proton-proton repulsion. In these conditions the interaction is accurately described by linear response theory. We have investigated the phase transitions occurring at relatively low temperature. For the ground state of classical protons, the fcc structure has been found to be the most favorable among several cubic and non-cubic structures, the bcc structure is only slightly higher in energy (or enthalpy) and found to be the stable crystal structure near melting. The melting and the fcc-bcc lines have been computed by free energy methods and located between 1500–3000 K and 200–1000 K, respectively. Our estimate of melting is in rough agreement with previous predictions based on the Lindemann criterium and *ab initio* Molecular Dynamics simulation of the electron-proton system.¹⁰ Quantum corrections to the melting transition have been computed by integration of the excess kinetic energy with respect to the inverse mass using kinetic energies obtained by PIMC. The melting line of hydrogen is barely affected by proton zero point motion at low density while the melting temperature is lowered by as much as 10% at the highest density considered. Quantum effects on the fcc-bcc transition line have not been considered because of the qualitative character of this prediction.

Our present results are relevant to the determination of the phase diagram of high pressure hydrogen, a system still largely unknown. In particular, the crystal structure of hydrogen in a region of phase diagram between $200 \text{ GPa} \leq p \leq 25 \text{ TPa}$ and $T \leq 2000 \text{ K}$, where several interesting physical phenomena occur (melting, molecular dissociation, metallization) is far from clear. Even the ground state structure and

its evolution with density from molecular to atomic hydrogen and beyond are unknown. A comprehensive search for lower energy/entropy structures, as has been recently reported²⁷ for protons interacting with DFT forces. In the present paper we have shown that even a simple pseudo-ion model contains a solid-solid phase transition. Our present results represent a starting point to trace the melting line and the solid-solid phase transition lines of atomic hydrogen from the high density side into the interesting lower density region. Work to extend at lower density the transition lines by coupled electron-ion Monte Carlo Method⁵⁷ is in progress.

ACKNOWLEDGMENTS

We have the pleasure to thank G. Ciccotti for his invaluable support, and S. Prestipino-Giaritta and F. Saija for useful discussions about the ground state structures. Computer resources were provided by CASPUR (Italy) within the Competitive HPC Initiative, Grant No.: cmp09-837, and by the DEISA Consortium (www.deisa.eu), co-funded through the EU FP6 project RI-031513 and the FP7 project RI-222919, through the DEISA Extreme Computing Initiative (DECI 2009). CP is supported by the MIUR, project PRIN2007 (Grant No. fw3mjx_004) and by IIT, project SEED n.259-SIMBEDD. DMC is supported by DOE Grant No. DE-FG52-09NA29456.

- ¹I. F. Silvera, *Rev. Mod. Phys.* **52**, 393 (1980).
- ²H. K. Mao and R. J. Hemley, *Rev. Mod. Phys.* **66**, 671 (1994).
- ³E. G. Maksimov and Yu I. Silov, *Phys. Usp.* **42**, 1121 (1999).
- ⁴T. Guillot, *Annu. Rev. Earth Planet Sci.* **33**, 493 (2005).
- ⁵P. Loubeyre, F. Occelli, and R. LeToullec, *Nature (London)* **416**, 613 (2002).
- ⁶E. Wigner and H. B. Huntington, *J. Chem. Phys.* **3**, 764 (1935).
- ⁷T. Weir, A. C. Mitchell, and W. J. Nellis, *Phys. Rev. Lett.* **76**, 1860 (1996).
- ⁸M. Städle and R. M. Martin, *Phys. Rev. Lett.* **84**, 6070 (2000).
- ⁹I. Goncharenko and P. Loubeyre, *Nature (London)* **435**, 1206 (2005).
- ¹⁰J. Kohanoff, *J. Low Temp. Phys.* **122**, 297 (2001).
- ¹¹S. Scandolo, *Proc. Natl. Acad. Sci. U.S.A.* **100**, 3051 (2003).
- ¹²S. A. Bonev, E. Schwegler, T. Ogitsu, and G. Galli, *Nature (London)* **431**, 669 (2004).
- ¹³I. Tamblyn and S. A. Bonev, *Phys. Rev. Lett.* **104**, 065702 (2010).
- ¹⁴W. Magro, D. M. Ceperley, C. Pierleoni, and B. Bernu, *Phys. Rev. Lett.* **76**, 1240 (1996).
- ¹⁵D. Saumon and G. Chabrier, *Phys. Rev. A* **46**, 2084 (1992).
- ¹⁶W. Ebeling and W. Richert, *Phys. Rev. A* **108**, 80 (1985).
- ¹⁷H. Kitamura and S. Ichimaru, *J. Phys. Soc. Jpn.* **67**, 950 (1998).
- ¹⁸D. Beule, W. Ebeling, A. Förster, H. Juranek, R. Redmer, and G. Röpke, *Phys. Rev. B* **59**, 14177 (1999).
- ¹⁹G. Chabrier, D. Saumon, and C. Winisdoerffer, *Astrophys. Space Sci.* **307**, 263 (2007).

- ²⁰M. A. Morales, C. Pierleoni, E. Schwegler, and D. M. Ceperley, *Proc. Natl. Acad. U.S.A.* **107**, 12799 (2010).
- ²¹K. T. Delaney, C. Pierleoni, and D. M. Ceperley, *Phys. Rev. Lett.* **97**, 235702 (2006).
- ²²V. E. Fortov, R. I. Ilkaev, V. A. Arinin, V. V. Burtzhev, V. A. Golubev, I. L. Iosilevskiy, V. V. Khrustalev, A. L. Mikhailov, M. A. Mochalov, V. Ya. Ternovoi, and M. V. Zhernokletov, *Phys. Rev. Lett.* **99**, 185001 (2007).
- ²³D. M. Ceperley and B. J. Alder, *Phys. Rev. E* **36**, 2092 (1987).
- ²⁴V. Natoli, R. M. Martin, and D. M. Ceperley, *Phys. Rev. Lett.* **70**, 1952 (1993).
- ²⁵V. Natoli, R. M. Martin, and D. M. Ceperley, *Phys. Rev. Lett.* **74**, 1601 (1995).
- ²⁶J. Kohanoff and J. P. Hansen, *Phys. Rev. E* **54**, 768 (1996).
- ²⁷J. M. McMahon and D. M. Ceperley, *Phys. Rev. Lett.* **106**, 165302 (2011).
- ²⁸E. Babaev, A. Sudbøand, and N. W. Ashcroft, *Nature London* **431**, 666 (2004).
- ²⁹J. Hammerberg and N. W. Ashcroft, *Phys. Rev. B* **9**, 409 (1974).
- ³⁰J. P. Hansen and I. R. McDonald, *Theory of Simple Liquids* (Academic, London, 1986).
- ³¹S. Ichimaru, H. Iyetomi, and S. Tanaka, *Phys. Rep.* **149**, 91 (1987); M. Baus and J. P. Hansen, *Phys. Rep.* **59**, 1 (1980).
- ³²D. M. Ceperley and B. J. Alder, *Phys. Rev. Lett.* **45**, 566 (1980).
- ³³G. Giuliani and G. Vignale, *Quantum Theory of Electron Liquids* (Cambridge University Press, Cambridge, 2005).
- ³⁴J. Perdew and A. Zunger, *Phys. Rev. B* **23**, 5048 (1981).
- ³⁵S. Moroni, D. M. Ceperley, and G. Senatore, *Phys. Rev. Lett.* **69**, 1837 (1992).
- ³⁶M. Corradini, R. Del Sole, G. Onida, and M. Palummo, *Phys. Rev. B* **57**, 14569 (1998).
- ³⁷K. S. Singwi and M. P. Tosi, *Solid State Phys.* **36** 177 (1981).
- ³⁸P. Ascarelli and R. Harrison, *Phys. Rev. Lett.* **22**, 285 (1969).
- ³⁹D. M. Ceperley, *Rev. Mod. Phys.* **67**, 279 (1995).
- ⁴⁰C. Pierleoni, K. T. Delaney, M. A. Morales, D. M. Ceperley, and M. Holzmann, *Comput. Phys. Commun.* **179**, 89 (2008).
- ⁴¹W. B. Hubbard and W. L. Slattery, *Astrophys. J.* **168**, 131 (1971).
- ⁴²S. Galam and J. P. Hansen, *Phys. Rev.* **148**, A816 (1976).
- ⁴³M. Ross, H. E. DeWitt, and W. B. Hubbard, *Phys. Rev. A* **24**, 1016 (1981).
- ⁴⁴H. Xu and J. P. Hansen, *Phys. Rev. E* **57**, 211 (1998).
- ⁴⁵G. Chabrier, *J. Phys. (France)* **51**, 1607 (1990).
- ⁴⁶M. Baus and C. F. Tejero, *Equilibrium Statistical Physics: Phases of Matter and Phase Transitions* (Springer, New York, 2008).
- ⁴⁷D. Frenkel and B. Smit, *Understanding Molecular Simulation*, 2nd ed. (Academic, London, 2002).
- ⁴⁸D. Frenkel and A. J. C. Ladd, *J. Chem. Phys.* **81**, 3188 (1984).
- ⁴⁹See the appendix of G. D'Adamo and C. Pierleoni, *J. Chem. Phys.* **133**, 204902 (2010).
- ⁵⁰G. S. Stringfellow, H. E. DeWitt, and W. L. Slattery, *Phys. Rev. A* **41**, 1105 (1990) and references therein.
- ⁵¹M. D. Jones and D. M. Ceperley, *Phys. Rev. Lett.* **76**, 4572 (1996).
- ⁵²B. Miltzer and R. L. Graham, *J. Phys. Chem. Solids* **67**, 2136 (2006).
- ⁵³C. Filippi and D. M. Ceperley, *Phys. Rev. B* **57**, 252 (1998).
- ⁵⁴E. Wigner, *Phys. Rev.* **40**, 749 (1932); J. G. Kirkwood, *Phys. Rev.* **44**, 31 (1933).
- ⁵⁵N. D. Drummond, M. D. Towler, and R. J. Needs, *Phys. Rev. B* **69**, 085116 (2004).
- ⁵⁶D. M. Ceperley, in *Simple Molecular Systems at Very High Pressure*, edited by A. Polian, P. Loubeyre, and N. Boccara (Plenum, 1988), p. 477.
- ⁵⁷E. Liberatore, M. A. Morales, C. Pierleoni, and D. M. Ceperley (in preparation).
- ⁵⁸in the case of hydrogen, the mass density in g/cm³ is related to the parameter r_s by: $\rho_m(\text{g/cm}^3) = 2.6946/r_s^3$.